Practical ppb-Level Room Temperature Chemiresistive Nitric Oxide Sensing Assembly Based on Ultrathin Thick Porphyrin MOF Nanosheets

Fu, Zijing; Chang, Yanwei; Chen, Zhuo; Xie, Huiming; Feng, Yancong; Wang, Yao; Gao, Yixun; Ren, Tao; French, Patrick J.; More Authors

DOI
10.1002/smll.202411264

Publication date
2025

Document Version
Final published version

Published in
Small

RESEARCH ARTICLE

NANO · MICRO small
www.small-journal.com

Practical ppb-Level Room Temperature Chemiresistive Nitric Oxide Sensing Assembly Based on Ultrathin Thick Porphyrin MOF Nanosheets

Zijing Fu, Yanwei Chang, Zhuo Chen, Huiming Xie, Yancong Feng, Fengnan Wang, Yao Wang, Hao Li, Yixun Gao,* Tao Ren,* Patrick J French, Ahmad Mohammad Umar Siddiqui, and Guofu Zhou*

Nitric oxide is an endogenous biological signaling molecule, and the corresponding fractional exhaled NO serves as an important indicator in clinical diagnostics and therapeutic applications. However, achieving accurate and rapid monitoring of ppb-level fractional exhaled nitric oxide (FeNO) at room temperature remains a significant challenge. Herein, ultrathin porphyrin metal–organic framework (MOF) sheets are selected to assemble with supramolecularly functionalized graphene sheets through hydrogen bonding and electrostatic interaction with 6 nm thickness. The resulting porphyrin MOF/graphene sheet-on-sheet nanohybrid is designed as a chemiresistive NO sensor which exhibits superior gas sensing performance at room temperature including an ultralow practical limit of detection (R_a/R_g = 1.047, 5 ppb NO), reliable repeatability, excellent selectivity against other exhaled gases, and relative long-term stability. Mechanism study indicates that the prominent NO sensing performance is attributed to the ordered framework of active sites of ferric-pyrrole (Fe—N_4) sites and less than 10 nm thick sheet-on-sheet heterojunction structure in the nanohybrid. The potential clinical utility of the obtained sensors is validated by exhalation tests toward exhalation samples from healthy individuals and asthma patients, respectively. This work provides an effective strategy of developing MOF-based room temperature ppb-level chemiresistive NO sensors for practical FeNO monitoring.

1. Introduction

As a significant biological signaling molecule,[1,2] the endogenous nitric oxide (NO) concentration may be affected to deviate from the standard values when there is an abnormality or lesion in the body, and then outwardly manifested as the fluctuation of fractional exhaled nitric oxide (FeNO).[3] Numerous studies have demonstrated the potential of FeNO analysis as a non-invasive assay for the diagnosis and treatment of respiratory inflammation, such as asthma.[4,5] Typically, healthy individuals exhibit less than 25 ppb NO in their breath, while asthmatic patients have levels exceeding 50 ppb.[6,7] Therefore, ppb-level NO detection holds distinct clinical value.

Traditional NO detection methods, including colorimetric analysis,[8] gas chromatography-mass spectrometry,[9] chemiluminescence techniques,[10] and electrochemical methods,[11] etc., are always constrained by drawbacks such as complex operating, expensive and bulky equipment. In recent years, metal oxide semiconductor

Z. Fu, Y. Chang, H. Xie, Y. Feng, Y. Wang, H. Li, Y. Gao, G. Zhou
Guangdong Provincial Key Laboratory of Optical Information Materials and Technology
Institute of Electronic Paper Displays
National Center for International Research on Green Optoelectronics
South China Academy of Advanced Optoelectronics
South China Normal University
Guangzhou 510006, P. R. China
E-mail: wangyao@m.scnu.edu.cn; gaoyixun@m.scnu.edu.cn

Z. Chen
Computer, Electrical and Mathematical Science and Engineering Division
King Abdullah University of Science and Technology (KAUST)
Thuwal 23955-6900, Saudi Arabia

F. Wang
Department of Thoracic Oncology
State Key Laboratory of Respiratory Diseases
The First Affiliated Hospital of Guangzhou Medical University
Guangzhou 510006, P. R. China

T. Ren
Department of Orthopedics
Zengcheng Campus
Nanfang Hospital
Southern Medical University
Guangzhou, Guangdong 510515, P. R. China
E-mail: nfyyrt@163.com

The ORCID identification number(s) for the author(s) of this article can be found under https://doi.org/10.1002/smll.202411264

DOI: 10.1002/smll.202411264

(MOS) based chemiresistive gas sensors have become the hotspot in the NO gas sensing field.[12–15] But essentially, the MOS-based sensors typically require a high working temperature to maintain oxygen species, including adsorbed oxygen ions and oxygen vacancies, which leads to excessive energy consumption and risky operation.[16,17] Besides, the poor selectivity of oxygen species restricts its practical application.

Some relevant research have illustrated the phenomenon that hemoglobin can recognize and bind NO selectively,[18] which is essentially an interaction between NO and the special heterocyclic chelating metal-pyrrole active site, resulting in changes in the geometry structure and electronic properties of the latter.[19,20] Currently, some studies using metal porphyrin derivatives or analogs for NO gas sensing detection.[21–23] However, the large conjugated electronic structure of porphyrin molecules causes a strong self-aggregate tendency, which shields most Metal-N_4 sites and thus reducing the NO binding efficiency.[24] A reasonable strategy is to orderly arrange porphyrin molecules as organic ligands within a metal–organic framework (MOF), which exhibits great potential for fabricating chemiresistive gas sensors at room temperature (RT).[25–30] The construction of a 3D network would allow abundant unoccupied Fe—N_4 sites to remain accessible for efficient NO binding.[31,32] Nevertheless, the poor electrical conductivity of isolated porphyrin MOF limits their chemiresistive response toward NO.[33–35] Integrating MOF with graphene, which is an ideal candidate material in the field of gas sensing, has been conducted as an effective way to obtain high specific surface area and electron conductivity.[36–45]

As shown in previous studies,[46–48] the sheet-on-sheet structure provides a larger contact area between the nanohybrid interface, which is conducive to the formation of stable heterojunctions with high carrier concentration and mobility at RT. Nevertheless, it remains difficult to achieve an ultralow practical limit of detection (pLOD) below 20 ppb for practical medical applications, because it is challenging to build an ultrathin sheet-on-sheet structure with a whole thickness less than 10 nm. In general, the layers of planar-grown porphyrin MOF structure severely tend to stack on each other, resulting in an excessively thicker sheet-on-sheet structure than 10 nm.[49] Therefore, it is of significance to find a strategy to achieving MOF-based heterojunctions with less than 10 nm thick sheet-on-sheet structure.[50]

In this work, a nanohybrid Al-TCPP(Fe) MOF/5-aminonaphthalene-1-sulfonic acid (ANS)-reduced graphene oxide (rGO) (abbr. AlTAG) was designed and synthesized by combining hydrothermal method and ultrasound-assisted method. A 6 nm thick Al-TCPP(Fe) Sheet (abbr. S-AlT) was obtained and then assembled with ANS-rGO. The obtained nanohybrids-based sensor exhibited superior sensing performance toward NO at RT including an ultralow pLOD (R_a/R_g = 1.047, 5 ppb NO). Its potential clinical utility was validated by exhalation tests toward exhalation samples from healthy individuals and asthma patients, respectively. Mechanism study indicated that the ordered framework of Fe—N_4 sites and less than 10 nm thick sheet-on-sheet heterojunction structure are mainly contributing to the superior sensing properties of the nanohybrid.

2. Results and Discussion

2.1. Preparation of the Sensing Material

Figures 1 and S28 (Supporting Information) illustrate the process flow for the preparation of the metalloporphyrin organic ligands with Fe—N_4 sites, Al-TCPP(Fe) MOFs in three morphologies, dipole molecule modified graphene sheets, and AlTAG nanohybrids based NO gas sensor. To integrate with ANS-rGO sheets perfectly and form large-area heterojunction, the ideal morphology of Al-TCPP(Fe) MOF is expected to be a 2D sheet with an ultrathin thickness and a relatively large lateral size. In this work, S-AlT were prepared by a bottom–up and top–down combination method, that is, a surfactant-assisted synthetic method with Cetyltrimethyl ammonium bromide (CTAB) as a morphology modifying auxiliary,[24,51] and an ultrasound-assisted exfoliation method. During the synthesis process, the cationic headgroup of CTAB will coordinate with the carboxyl group exposed at the margin of Al-TCPP(Fe) MOF and leave its alkyl chain on another side, and then the coordination between the two will prevent the frontal stacking effect and refrain from the overgrowth of Al-TCPP(Fe) MOF in its longitudinal direction.[52] That results in the reduced in-plane stacking and the increased anisotropic growth of Al-TCPP(Fe) MOF lamellae, as well as end-capping of the monoacids, leading to ultrathin sheet layer secondary structures.[24,53] Ultimately, a 6 nm ultrathin Al-TCPP(Fe) sheet was obtained and integrated with ANS-rGO to construct ultrathin sheet-on-sheet S-AlTAG nanohybrid.

2.2. Morphology and Structure Characterizations

The dimension and morphology of the synthesized samples were characterized by scanning electron microscopy (SEM) and transmission electron microscopy (TEM). The significant differences of the morphologically regulated Al-TCPP(Fe) MOFs can be observed according to SEM images, in which Al-TCPP(Fe) Bulk (abbr. B-AlT) is a micron-sized random mass (Figure S1a, Supporting Information), Al-TCPP(Fe) Cara (abbr. C-AlT) is a jujube stone-like shape with a diameter of 1–1.5 µm and a length of 1.5–2 µm (Figure S1b,c, Supporting Information), and S-AlT is a sheet with a 160 nm average diameter (**Figure 2a**) calculated by Gaussian fitting (Figure S2, Supporting Information). Furthermore, the average thickness of S-AlT is confirmed to be 6 nm by atomic force microscopy (AFM). (Figure S3a, Supporting Information). The structural details of S-AlT are further investigated with TEM as shown in Figure 2d, which clearly demonstrates

P. J French
BE Laboratory
EWI
Delft University of Technology
Delft 2628CD, The Netherlands
A. M. U. Siddiqui
Department of Chemistry
Faculty of Science and Arts and Promising Centre for Sensors and Electronic Devices (PCSED)
Najran University
Najran 11001, Saudi Arabia
Z. Chen
Hebei Onlysense Technology Co., Ltd
Tangshan 063000, China

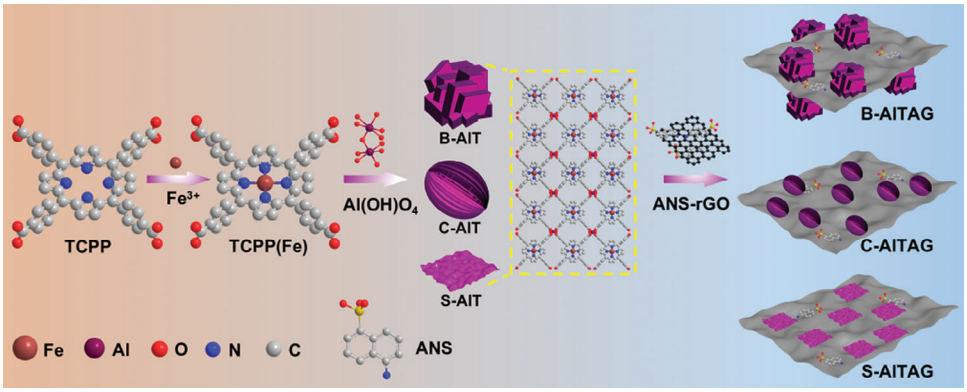

Figure 1. Schematic diagram of the preparation process of Al-TCPP(Fe) MOFs and AlTAG nanohybrids.

that the lattice fringe (Figure 2e) with a spacing of 1.6 nm corresponds to the (100) crystal plane (Figure 2f) of Al-TCPP MOF. As shown in Figure S4 (Supporting Information), the high-angle annular dark-field scanning transmission electron microscopy (HAADF STEM) image and the corresponding energy dispersive X-ray spectroscopy (EDS) mapping patterns of S-AlT were obtained, which clearly illustrates the homogeneous distribution of Al, Fe, O, C, and N elements, indicating the successful preparation of S-AlT. The microstructure of ANS-rGO is typical graphene sheets (Figure 2b; Figure S1d,e, Supporting Information) with a 4 nm thickness evidenced by AFM height profile (Figure S3b, Supporting Information). This result showed that the introduction of ANS on graphene could effectively avoid the self-stacking of graphene owing to the charge repel effect of the negative sulfonic groups, referring to our previous works.[42,43] As shown in Figure 2c and Figure S1f (Supporting Information), the prepared S-AlTAG-*M* nanohybrid (*M* represents the mass ratio between S-AlT and ANS-rGO, $M = M_{\text{S-AlT}}/M_{\text{ANS-rGO}}$, etc.) was derived from the successful assembly of S-AlT with ANS/rGO sheets, and the total thickness of the nanohybrid multilayer is ≈11.7 nm (Figure S3c, Supporting Information).

To further analyze the crystalline structure, all the as-prepared Al-TCPP(Fe) MOFs were examined by powder X-ray diffraction (PXRD) analysis (Figure 2g). Al-TCPP(Fe) MOFs with different

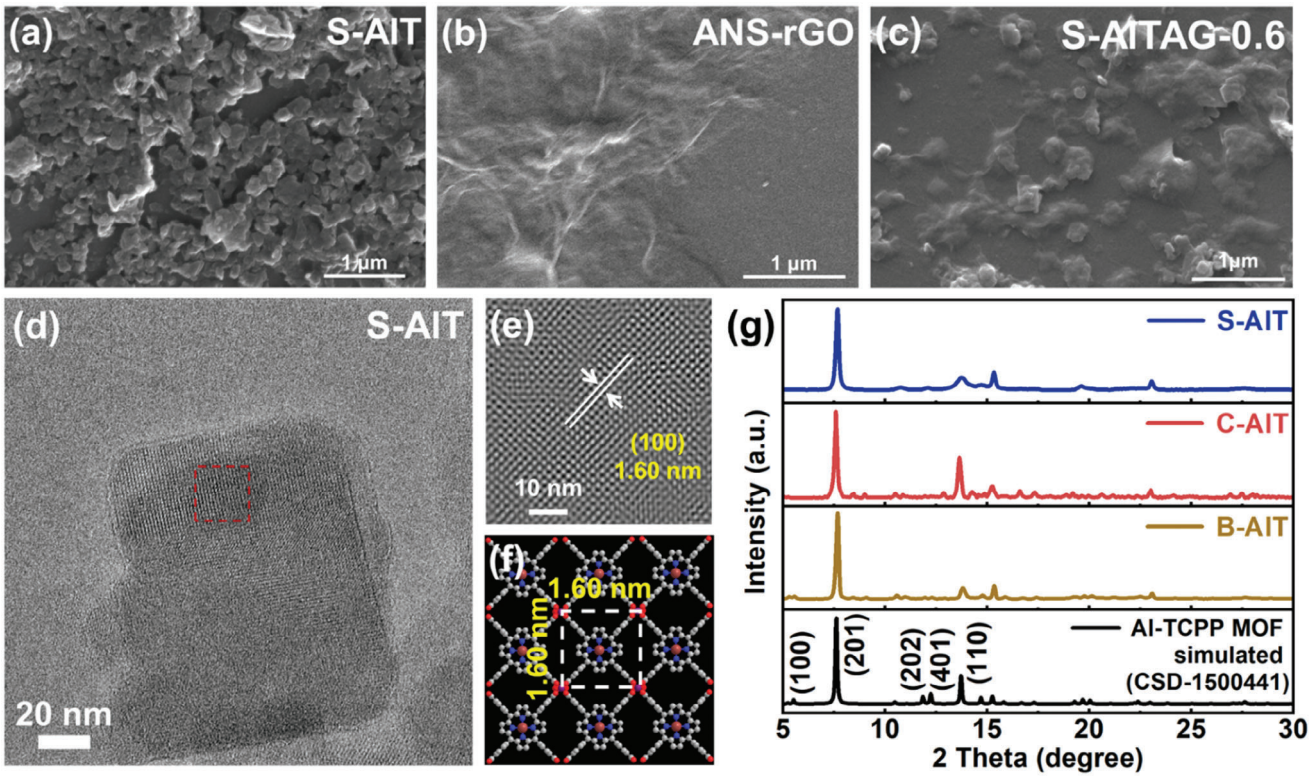

Figure 2. SEM images of a) S-AlT, b) ANS-rGO, and c) S-AlTAG-0.6. d,e) TEM images of S-AlT. f) The (100) crystal plane of Al-TCPP(Fe) MOF. g) XRD patterns of Al-TCPP MOF simulated, B-AlT, C-AlT, and S-AlT.

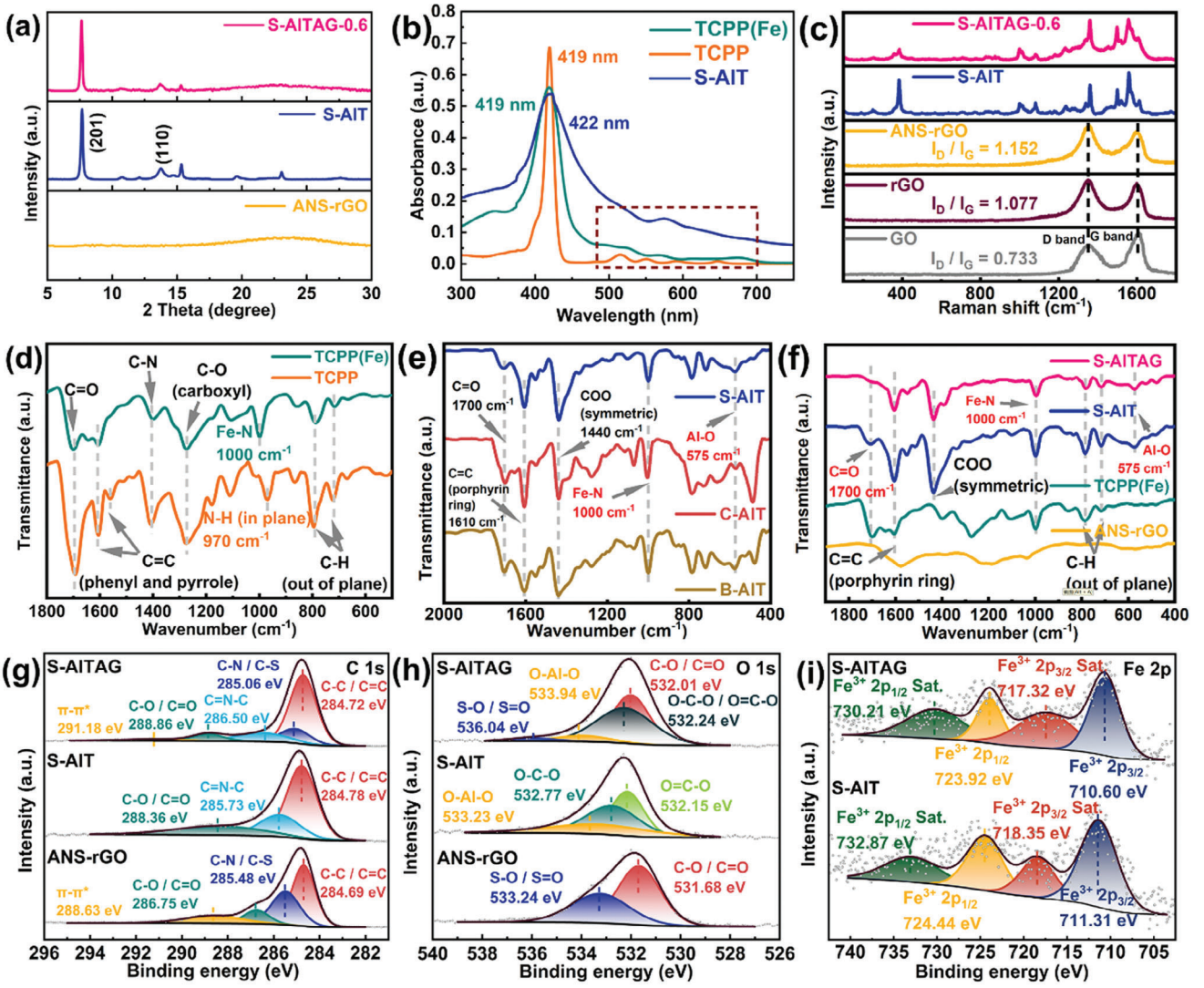

Figure 3. a) XRD patterns of ANS-rGO, S-AIT, and S-AITAG-0.6. b) UV–vis absorption spectrum image of TCPP, TCPP(Fe), and S-AIT. c) Raman spectroscopy images of ANS-rGO, S-AIT, and S-AITAG-0.6. Fourier Transform Infrared (FT-IR) spectroscopy images of d) TCPP and TCPP(Fe), e) B-AIT, C-AIT, and S-AIT, f) ANS-rGO, TCPP(Fe), S-AIT, and S-AITAG-0.6. XPS high-resolution spectra of g) C 1s, h) O 1s, i) Fe 2p of ANS-rGO, TCPP(Fe), S-AIT, and S-AITAG-0.6.

microstructures are consistent with the standard diffraction peak spectrum of Al-TCPP MOF (CSD-1500441) in the diffraction peak shape and position. The peaks of Al-TCPP(Fe) MOFs at 2θ of 5.54°, 7.67°, 11.88°, 12.27°, and 13.78° match with the crystal faces of (100), (201), (202), (401), and (110), respectively. The Al-TCPP(Fe) MOFs orthorhombic system is consistent with the *Cmmm* space groups.[54] The typical peaks of 7.67° and 13.78° indicate the formation of the $Al(OH)O_4$ chain metal nodes bonded with four TCPP(Fe) organic ligands, a common motif with octahedral symmetry for M^{3+} frameworks with carboxylate ligands (Figures S5, and S6, Supporting Information),[55,56] which are the elementary unit for the construction of three-dimension spatial coordination Al-TCPP(Fe) MOF. After assembling with ANS-rGO sheets, the diffraction spectrum of S-AITAG exhibits such a broad peak in the same position as ANS-rGO in the range from 15° to 30° that some weak peaks of S-AIT are cloaked (**Figure** 3a).

The central coordination of porphyrin ligand was typically studied by UV–vis absorption spectroscopy. The corresponding signals are shown in Figure 3b and Figure S7 (Supporting Information), which demonstrate the typical variation of the sharp Soret and Q bands arising from π–π^* transitions, namely consistent with the transition from the ground (S_0) state to the second (S_2) and the first (S_1) excited states, respectively.[57] Considering TCPP, the strong characteristic absorption is observed at 419 nm (Soret band), and the four weak absorptions in the range of 500–700 nm (Q band), including 515 nm (λ_1), 550 nm (λ_2), 591 nm(λ_3) and 647 nm (λ_4).[58] Compared to that, the phenomenon is different in the spectrum of TCPP(Fe). Despite the Soret band remaining essentially unchanged, all the absorption peaks in the Q band disappear except λ_2 still present, which is red-shifted from 550 nm to 567 nm, revealing that the structure symmetry enhancement of the porphyrin ring after the N—H bonds are replaced

by Fe—N bonds.[59,60] In addition, the Soret band of TCPP(Fe) at 419 nm shows a slight red-shift (422 nm) in S-AlT,[55] proving TCPP(Fe) organic ligands are compelled to adopt side-to-side and face-to-face aggregation modes.[61] The active Fe—N_4 sites have been integrated orderly by building the spatial MOF coordination networks.

The series of graphene derivatives were characterized by Raman spectroscopy. As exhibited in Figure 3c, The D-band at 1350 cm^{-1} is associated with the breathing mode of κ-point phonons of A_{1g} symmetry in graphene, and the G-band 1600 cm^{-1} is related to the first-order scattering of the E_{2g} mode of the sp^2 bonds of carbon atoms. The I_D/I_G values of the as-prepared rGO and ANS/rGO are 1.077 and 1.152, respectively, which are all higher than that of graphene oxide (GO) (0.733), indicating that GO has been successfully reduced and functionalized.[62] Apart from that, many characteristic bands arise in the spectrum of S-AlTAG at a range of 900–1700 cm^{-1}, which are ascribed to S-AlT. The modes at 1081.39 ($\nu_{as(Ca\text{-}N)}$), 1233.74 ($\nu_{(Cm\text{-}Ph)}$), 1359.74 ($\nu_{s(Ca\text{-}N)}$), 1498.34 ($\nu_{s(Ca\text{-}Cm)}$), 1556.94 ($\nu_{(Cb\text{-}Cb)}$), and 1573.13 cm^{-1} ($\nu_{(Cb\text{-}Cb)}$) are attributed to the porphyrin core in-plane mode.[63,64] Moreover, the mode at 892.20 ($\nu_{(Ph)}$), 1011.88 ($\delta_{(Ph)}$), and 1607.03 cm^{-1} ($\delta_{(Ph)}$) are assigned to the phenyl ring in-plane mode. The intensity of the typical Raman peak at 383.98 cm^{-1} ($\nu_{(Fe\text{-}N)}$), ascribed to the stretching vibration of the Fe—N bond, weakens after compositing (Figure S8a, Supporting Information), which is interpreted as electrostatic interaction between the positively charged central iron element of S-AlT interface and the negatively charged ANS-rGO.[65] That inference can also be demonstrated by the fact that S-AlT and ANS-rGO show opposite Zeta potential (Figure S25, Supporting Information). On account of the two broad peaks the D band and G band coinciding with S-AlT in the range of 1300–1700 cm^{-1}, the full width at half maximum in the Raman spectrum of S-AlTAG becomes widened (Figure S8b, Supporting Information). More detailed Raman peak information is tabulated in Table S2 (Supporting Information).

Fourier transform infrared spectroscopy (FT-IR) spectroscopy was performed to demonstrate the successful preparation of the organic ligand TCPP(Fe), Al-TCPP(Fe) MOFs, ANS-rGO, and AlTAG nanohybrids. As illustrated in Figure S10a (Supporting Information) and Figure 3d, the distinctive absorption peaks of TCPP at 970 and 3315 cm^{-1} are severally credited to the N—H in-plane vibration of the benzene ring and stretching vibration, which are both vanished in the absorption spectrum of TCPP(Fe).[32] Instead of that a new absorption peak appeared at 1000 cm^{-1} featuring the characteristic stretching/bending vibration of the Fe—N bond, illustrating that the Fe (III) ion was chelated into the porphyrin ring, meanwhile TCPP was converted to TCPP(Fe) organic ligand.[66,67] Figures S10b (Supporting Information) and Figure 3e showed the FT-IR spectra of different Al-TCPP(Fe) MOFs. The depression of C═O (1700 cm^{-1}) caused by the coordination of carboxy groups with Al ions, and the prominent emergence of Fe—N (1000 cm^{-1}) and Al—O (575 cm^{-1}), revealing the establishment of the $Al(OH)O_4$ chain metal node unit cells and proving the successful synthesis of Al-TCPP(Fe) MOFs.[44] The oxygen-containing functional groups of GO displayed in Figure S10c (Supporting Information) are consistent with the presence of absorption peaks (O—H, 3410 cm^{-1}; C═O,1740 cm^{-1}; C—OH, 1240 cm^{-1}; C—O—C (epoxy group), 1080 cm^{-1}), which aren't found in rGO, indicating that GO is reduced successfully.[68,69] In comparison with rGO, the broader peak at 3400 cm^{-1} of ANS-rGO can be attributed to N—H bond stretching vibration from the ANS molecule, and the conspicuous absorption band in the 1200–1030 cm^{-1} range is ascribed to S═O bond stretching vibration of sulfonic acid groups, suggesting the self-assembly of rGO with the ANS molecule.[42] Afterward, the infrared absorption information of the gas-sensing nanohybrid is described in Figure S10d (Supporting Information) and Figure 3f. Significantly, the further weakening and red-shifting of the C═O absorption peak for S-AlTAG compared to S-AlT suggests that the uncoordinated carboxy groups at the margin of S-AlT are consumed for the assembly process with ANS-rGO. Consequently, one of the predominant driving forces of the S-AlTAG self-assembly should be the hydrogen bond interaction, which allows the interfacial arrangement of the nanohybrid to overcome lattice misfit dislocation and symmetry imbalances and promote dispersion of the electronic states in the active center.[70,71]

X-ray photoelectron spectroscopy (XPS) was adopted to measure the chemical element composition and the surface valence states. The full XPS survey scan spectra calibrated with C 1s at 284.8 eV are shown in Figure S11a (Supporting Information) for pure ANS-rGO, S-AlT, and S-AlTAG, reflecting that they consist of several elements including C, N, O, S, Fe, and Al. The presence of hydrogen bond interaction is precisely detected from a series of orbital levels. The C 1s spectrum of ANS-rGO can be deconvoluted into four different components (Figure 3g). The bands at 284.69, 285.48, 286.75, and 288.63 eV are assigned to the C—C/C═C in the porphyrin rings, C—N/C—S of ANS molecule, C—O/C═O of the carbonyl or carboxylic acidic and π–π* transition, respectively.[72] Remarkably, after assembling with S-AlT, the π–π* transition peak position shifted slightly toward the higher binding energy and its almost disappearance of the absorption intensity describing that the feeble interaction of ANS-rGO itself is further weakened to nearly eliminate.[73] A new C═N—C absorption peak of deprotonated coordination pyrrolic N in the porphyrin rings located at 286.50 eV emerges in the C 1s spectrum of S-AlTAG proving that the successful preparation of S-AlTAG nanohybrid. Through the analysis of the O1s orbital (Figure 3h), it can be found that characteristic peaks of S—O/S═O bond from ANS-rGO at 536.04 eV and O—Al—O bond from S-AlT at 533.94 eV coexist in the nanohybrid, which is consistent with the FT-IR spectra analysis confirming the assembly of ANS-rGO and S-AlT.[74] The N 1s core level of S-AlT could be decomposed into three peaks centered at 398.70, 399.88, and 404.48 eV(Figure S11b, Supporting Information), which correspond to C═N, C—N, and Fe—N bonds, respectively. The binding energy of the Fe—N bond in the nanohybrid takes a mild up-shift in comparison with S-AlT, further verifying the formation of electrostatic interaction between the positively charged central iron element and the negatively charged ANS-rGO.[52] That conclusion can also be validated by the overall slight down-shift of S-AlTAG absorption peaks in Fe 2p spectra(Figure 3i) compared to S-AlT, which include Fe—N $2p_{3/2}$ (710.60 eV) and Fe—N $2p_{1/2}$ (723.92 eV) accompanied by their satellite peaks are attributed to the spin-orbit coupling of Fe $2p_{3/2}$ and Fe $2p_{1/2}$, respectively.[67,75] (See details in Supporting Information). In summary, it has been verified and characterized that, except for the hydrothermal synthesis of MOFs, the

formation of the final composite of Porphyrin MOF/ANS-rGO is based on multiple supramolecular interactions including hydrogen bonding and electrostatic interactions.

2.3. Nitric Oxide Sensing Performance

To investigate NO sensing properties, a series of RT gas sensors were fabricated on the interdigital electrodes (IDEs) by drop casting method with the as-prepared B-AlTAG, C-AlTAG, and S-AlTAG used as the sensing materials. The current versus voltage (*I–V*) characteristics curves of the ppb-level RT gas sensors are performed as shown in Figure S12 (Supporting Information). The excellent linearity revealed an ohmic contact between the gas sensing materials and the IDEs, which excluded the influence factor of the electrode patch.[76] All the gas sensing performance measurements were conducted at RT with N_2 as the background gas for the response process. In addition, the sensor's conductivity in response to NO is greater relative to the background atmosphere, suggesting that the sensing materials have p-type semiconductor characteristics, which is further confirmed by subsequent experiments.

It is learned that the mass ratio of Al-TCPP(Fe) MOF to ANS-rGO is one of the decisive factors in AlTAG-*M* ($M = M_{\text{Al-TCPP(Fe) MOF}}/M_{\text{ANS-rGO}}$) based gas sensor performance, and the optimal condition for obtaining high sensing performance is explored by controlling the mass ratio of the two. First, due to the intrinsic property of extremely low conductivity of Al-TCPP(Fe) MOF, the sensor prepared directly from it for the response process exhibited an almost zero baseline and few electrical signal changes to capture. Meanwhile, the pure ANS-rGO sensor showed only a low response to 10 ppm NO ($R_a/R_g = 1.787$). **Figure** 4a demonstrates the typical response magnification-mass ratio variation plot. As the increasing mass ratio, the response value (*S*) shows a tendency from rising to declining, with the maximum response value (Max $R_a/R_g = 8.349$) corresponding to a mass ratio is 0.6 (S-AlTAG-0.6, $M = M_{\text{S-AlT}}/M_{\text{ANS-rGO}} = 0.6$). Obviously, as displayed in Figure 4b, S-AlT is heavily encapsulated by ANS-rGO in the low mass ratio range ($M = 0.05$–0.2), leading to most Fe—N_4 sites being hard to specifically combine with NO, and the decreasing effective electron transfer density is in turn reflected as the relatively tiny electrical signal response values. However, in the high mass ratio range ($M = 1$–3), the electrical characteristics of the sensor are determined principally by S-AlT. With the decreasing proportion of ANS-rGO, its surface anchors extensive S-AlT until it is completely encased, at which time the conductivity of S-AlTAG decreases drastically, and the sensor exhibits an imperceptible change of electrical signals in the NO atmosphere. Particularly, the S-AlTAG-0.6-based sensor has a high response value with speedy and ample response/recovery, which derives from the optimum mass ratio condition.

An instantaneous response/recovery processing characteristics of the sensor are crucial similarly. As demonstrated in Figure 4c, the response/recovery time of S-AlTAG-0.6 based sensor toward 10 ppm NO is 80 s/20 s, respectively. It also reaches a desirable standard even in the ppb level concentration range shown in Figure S13c,d (Supporting Information), and other response/recovery time data toward a low concentration NO are tabulated (Table S3, Supporting Information). That is ascribed to the NO specific binding Fe—N_4 sites, the ultrathin sheet-on-sheet morphology and the large-area heterojunction strengthen the density and speed of charge transfer. Beyond that, the response/recovery time of the S-AlTAG-0.6-based sensor is shorter than B-AlTAG-0.6 and C-AlTAG-0.6-based sensors (Figure S13a,b, Supporting Information). Collectively, the resistance of those AlTAG-based sensors decreases rapidly after being exposed to NO and returns to the initial value after the measured gas release, showing p-type semiconductor sensing characteristics.

Furthermore, Figure S14a (Supporting Information) displays five response-recovery cycles of S-AlTAG-0.6 based sensor toward 10 ppm NO to verify its repeatability. The response values of each NO sensing cycle are constant without an obvious baseline drift, and the specific rate of change in the repeatability test is 2.5%, 1.8%, −3.1%, 0.6%, and −1.8% respectively with a standard deviation of 0.18, indicating that the sensor has ideal repeatability and recoverability (see the Supporting Information for details). The identically excellent performance occurs in response-recovery cycles of the sensor toward 10 ppb NO and 5 ppb exhibited in Figure S14b,c (Supporting Information). Oppositely, B-AlTAG-0.6, and C-AlTAG-0.6 based sensors both display a low response value to 10 ppm NO with a not neglectable baseline drift (Figure 4d), revealing that S-AlTAG-0.6 based sensor occupies favorable ultrathin sheet-on-sheet morphology factor for charge transfer in the gas sensing process.

Figure 4e shows the response-recovery curves of the S-AlTAG-0.6-based sensor exposed to different concentrations of NO at RT. A series of obvious response signals can be received even at a low concentration of 5 ppb NO (Figure S15a, Supporting Information), indicating that the sensor has an extremely low practical limit of detection (pLOD) for the trace NO analysis. A positive linear relationship of the response value versus NO concentration (0.1–10 ppm) with high confidence is exhibited in Figure 4f, whose linear regression curve equation is represented as $y = 1.40900 + 0.69299x$ (y, sensor response value; x, target gas concentration) with a regression coefficient (R^2) of 0.99335. To better reflect the relationship between the response value and the low concentration gradient interval, an additional linear regression curve is fitted in the 5–100 ppb range (Figure S15b, Supporting Information). However, as shown in Figure S15c–f (Supporting Information), the pLOD of B-AlTAG-0.6 and C-AlTAG-0.6 based sensors are 500 and 100 ppb NO, respectively. Besides, since both suffer from baseline drift triggered by inferior recoverability, their response values display an inadequate positive linear relationship with the concentration gradient. Additionally, the theoretical limit of detection (tLOD) of the S-AlTAG-0.6-based sensor is calculated to be 1.13 ppb based on the root-mean-square noise amplitude (rms_{noise}) (see the Supporting Information for calculation details). A sensing performance comparison of the typical NO sensors reported in recent years is summarized in Table S4 (Supporting Information). It is worth noting that the sensor in this work exhibits the lowest pLOD (5 ppb). Overall, the S-AlTAG-0.6-based sensor shows an extraordinary competitive advantage in the field of ppb-level NO detection at RT, which makes it a promising practical application of clinical FeNO prober for respiratory disease diagnosis and treatment.

It is necessary for the sensor to possess selectivity to distinguish the target gas in clinical applications on account

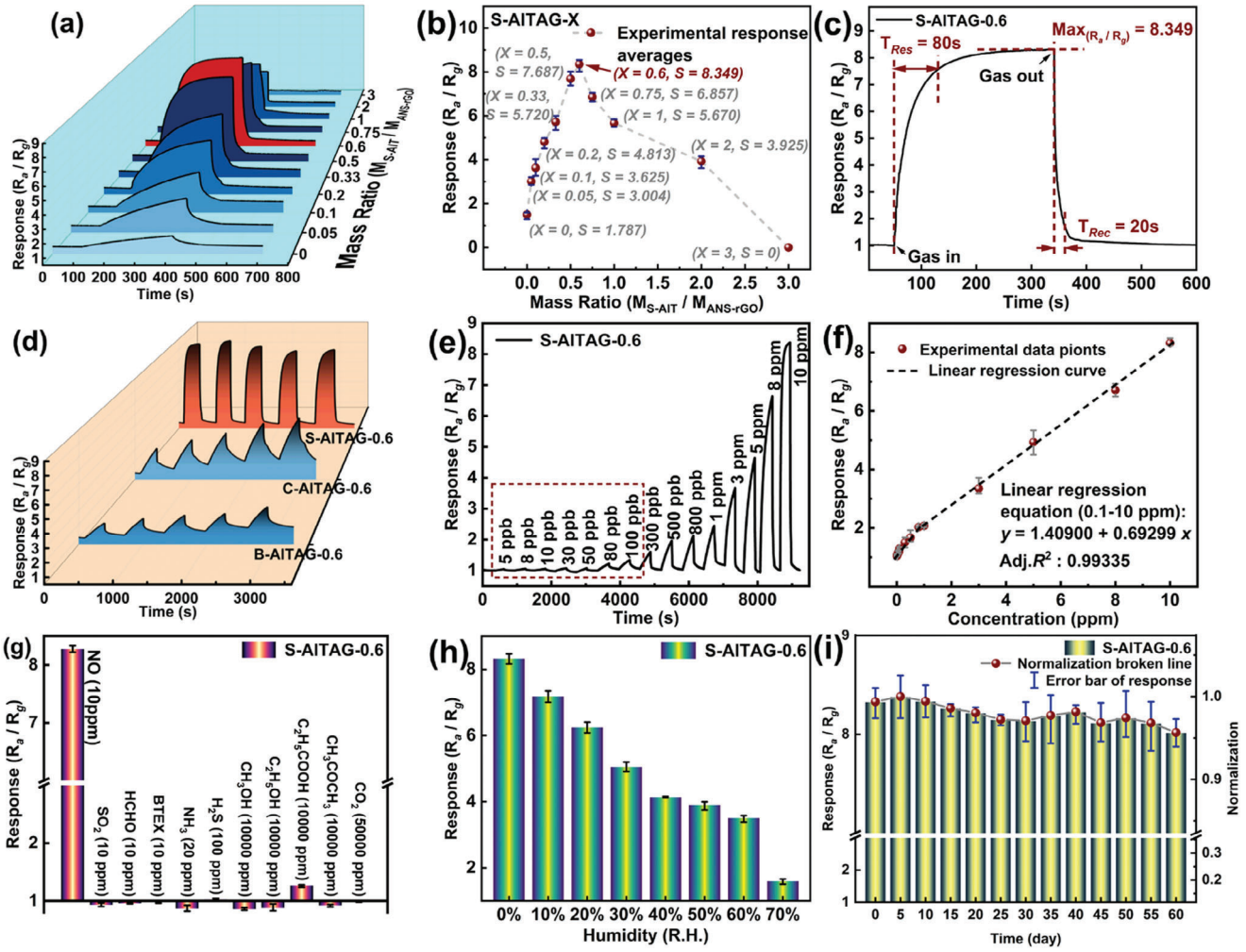

Figure 4. a) Typical response curves of S-AlTAG-*M* ($M = M_{S\text{-}AlT}/M_{ANS\text{-}rGO}$, M = 0, 0.05, 0.1, 0.2, 0.33, 0.5, 0.6, 0.75, 1, 2, and 3) based sensor toward 10 ppm NO, and b) the corresponding response-mass ratio plot. c) Real-time response/recovery curve at RT of S-AlTAG-0.6 based sensor toward 10 ppm NO. d) Repeatability response curves of B-AlTAG-0.6, C-AlTAG-0.6, and S-AlTAG-0.6 based sensor toward 10 ppm NO over five cycles. e) Gradient response curves of S-AlTAG-0.6 based sensor toward NO at different concentrations from 5 to 10 ppm, and f) the corresponding fitted linear regression curve. g) The selectivity of the S-AlTAG-0.6-based sensor toward various gases at corresponding concentrations. h) The response of the S-AlTAG-0.6-based sensor toward 10 ppm NO at different relative humidities ranging from 0% to 70% at room temperature. i) Long-term stability of S-AlTAG-0.6 based sensor exposed toward 10 ppm NO at room temperature.

of the sundry complex compositions in human exhaled breath.[77,78] Illustrating in Figure 4g, the gas selectivity of S-AlTAG-0.6 based sensor is investigated by exposure it to 10 ppm NO or various high concentrations of interfering gases, including ammonia (NH_3; R_g/R_a = 1.156, 20 ppm), sulfur dioxide (SO_2; R_g/R_a = 1.073, 10 ppm), hydrogen sulfide (H_2S; R_a/R_g = 1.025, 100 ppm), carbon dioxide (CO_2; R_g/R_a = 1.010, 50 000 ppm), formaldehyde (HCHO; R_g/R_a = 1.045, 10 ppm), methanol (CH_3OH; R_g/R_a = 1.166, 10 000 ppm), ethanol (C_2H_5OH; R_g/R_a = 1.139, 10 000 ppm), ethanoic acid (CH_3COOH; R_a/R_g = 1.266, 10 000 ppm), acetone (CH_3COCH_3; R_g/R_a = 1.083, 10 000 ppm), BTEX (a mixture of gases, including benzene, toluene, ethylbenzene, and o-xylene; R_g/R_a = 1.024, 10 ppm) (Figure S16a,b, Supporting Information). The tremendous selectivity of the sensor can be attributed to the Fe-N_4 sites binding NO specifically.

To investigate the humidity effect, the S-AlTAG-0.6-based sensor was exposed to different relative humidity (RH) from 0% to 70%, and the corresponding response value toward 10 ppm NO is recorded (Figure 4h). As the RH increases, the sensor performance is dramatically affected as evidenced by a severe dip in the response values, that is, which corresponds to 10%, 20%, 30%, 40%, 50%, 60%, and 70% RH is 8.325, 7.182, 6.242, 5.049, 4.139, 3.905, 3.504, and 1.595, respectively. Once the RH reaches 40%, the sensor's response value will halve. The phenomenon of being non-resistant to humidity may be interpreted as the competition between water molecules and NO absorbed on the sensing layer surface. This dilemma can be addressed by the technology of drying the imported gas in advance, analogous to what has been developed maturely in modern exhaled breath detection. Although the sensing performance of the S-AlTAG-0.6-based sensor is suppressed under high RH, it will regain rapidly once switching to

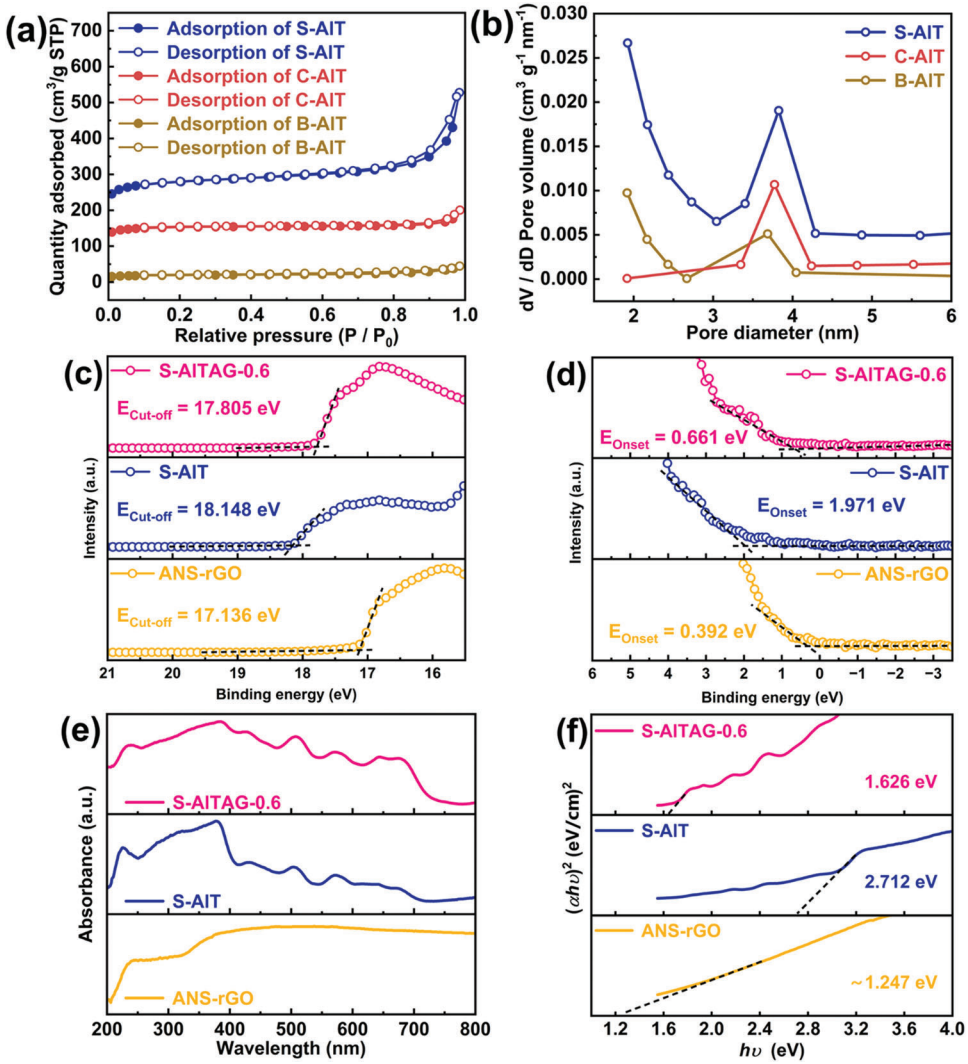

Figure 5. a) N_2 adsorption/desorption isotherms and b) pore size distribution of B-AlTAG, C-AlTAG, and S-AlTAG. c) Secondary electron emission spectra, d) Valence band spectra, e) UV–vis diffuse reflectance spectroscopy (UV–vis DRS) image, and f) Tauc plots of ANS-rGO, S-AlT, and S-AlTAG-0.6.

a drying atmosphere, indicating that the sensor is still stable toward humidity in a sense (Figure S17, Supporting Information).

To demonstrate that the sensor has a long service life to meet the requirement in practical applications, the fluctuation degree in the long-term stability of the sensor is investigated and characterized by a standard deviation. In Figure 4i, the response of the sensor for 10 ppm NO is found to be slightly decreased (3.75%) after 60 days of testing with a standard deviation of 0.010. Similarly, the response for 10 ppb NO shows a decrease of 2.31% in response value after 30 days of testing with a standard deviation of 0.099(Figure S18, Supporting Information), indicating the relatively high long-term stability of S-AlTAG-0.6 based sensor (see the Supporting Information for details).

In summary, the specific NO binding Fe—N_4 active sites spatial network structure, the ultrathin sheet-on-sheet structure of S-AlTAG with high specific surface area and high porosity, and the large-area heterojunction established as an electron-transfer bridge on the interface, all of these collectively contribute to the sensor's distinguished sensing performance.

2.4. Nitric Oxide Sensing Mechanism

First, as for the NO gas mass transfer process, the ultrathin S-AlT occupies a significant advantage over the other two morphology Al-TCPP(Fe) MOFs. The N_2 adsorption/desorption isothermal analyses at 77 K were carried out to evaluate the porous properties. **Figure** 5a shows that Al-TCPP(Fe) MOFs revealed a reversible typical type I N_2 isotherm physisorption behavior, with the adsorption and desorption branches closed without hysteresis. The calculated surface area of S-AlT is 896.3267 and 1722.9673 $m^2 g^{-1}$ using the Brunauer–Emmett–Teller model and the Langmuir model, respectively, much higher than the corresponding values of B-AlT and C-AlT (Figure S20a, Supporting Information). As displayed in Figure 5b and S-AlT possesses the main pore size of ≈3.8 nm, which possibly should be attributed to its random aggregation. Herein, what needs to be pointed out is that there existed pores of relatively small size (<2 nm), ascribing to the surface pores of S-AlT. The adsorption/desorption cumulative pore volume of S-AlT is 0.433075 and

0.433560 cm^3 g^{-1} using the Barrett–Joiner–Halenda model, respectively, much higher than B-AlT and C-AlT (Figure S20b, Supporting Information). Comprehensively, the superiority of high specific surface area and porosity makes the ultrathin S-AlT possess preferable accumulation and mass transfer capabilities for NO gas sensing,[53] and therefore S-AlTAG based sensors equip higher responsiveness and response-recovery rate.

Based on charge transfer theory and energy band theory, a mechanism for heterojunction enhanced NO gas sensing in S-AlTAG-0.6 based sensor was proposed. The improved sensing performance of the nanohybrid can be attributed to the formation of large-area heterojunction and the more efficient charge transfer from the band structure changes.

UV photoelectron spectroscopy (UPS) is obtained to confirm the work functions (Φ, the minimum energy required for an electron to transition from the Fermi level (E_f) to the vacuum level (E_{vac})) and the valence band top position of ANS-rGO, S-AlT, and S-AlTAG-0.6, which is used to determine the band structure and the charge transfer details of them.[72,79] The secondary electron emission spectra (Figure 5c) and valence band spectra (Figure 5d) are derived from the spectrum in Figure S21 (Supporting Information). The Fermi level (E_f) position is extracted from the cut-off energy ($E_{cut\text{-}off}$) of the secondary electron emission spectra as the following equation:

$$\Phi = E_f = 21.22\ \text{eV} - E_{cut-off} \quad (1)$$

Then, the valence band top (E_v) position with reference to the Fermi level is inferred from the onset energy (E_{onset}) of the valence band edge as the following equation:

$$E_v = 21.22\ \text{eV} - E_{cut-off} + E_{onset} \quad (2)$$

where 21.22 eV is the photon energy of the He I light source, $E_{cut\text{-}off}$ and E_{onset} can be concluded from the intercept of the two tangent lines in the *x*-axis. Therefore, the work functions (Φ) of ANS-rGO, S-AlT, and S-AlTAG-0.6 are calculated to be 4.084, 3.072, and 3.415 eV, similarly, the valence band top positions of the three are 4.476, 5.043, and 4.076 eV, respectively. The larger work function of ANS-rGO compared with S-AlT indicates that the electrons are transferred from the latter to the former in the heterojunction.

UV–vis DRS is recorded to estimate the band gaps of ANS-rGO, S-AlT, and S-AlTAG-0.6. The absorption in Figure 5e qualitatively determines that the band gap of S-AlT is wider than that of S-AlTAG-0.6, indicating that charge transfer from the valence band top to the conduction band bottom becomes readily in S-AlTAG-0.6. Besides, the band gaps can be quantitatively calculated by the following Kubelka–Munk function equation:[44,80]

$$(\alpha h\upsilon)^n = A\left(h\upsilon - E_g\right) \quad (3)$$

where α, h, υ, A, and E_g are the absorption coefficient, Planck's constant, incident photon frequency, proportionality constant, and band gap energy, respectively. For a direct bandgap semiconductor, the value of n is 2. The resulting Tauc plots are exhibited in Figure S22 (Supporting Information), and E_g is identically figured out from the intercept of the two tangent lines in the *x*-axis. Hence, the band gaps (E_g) of S-AlT, S-AlTAG-0.6, and ANS-rGO are calculated to be 2.712, 1.626, and ≈1.247 eV, respectively (Figure 5f). Moreover, the conduction band bottom (E_c) position with reference to the Fermi level is deduced from the valence band top position and the band gap energy as the following equation:

$$E_c = E_v + E_g \quad (4)$$

Then, the conduction band bottom positions of the three above are 3.229, 2.331, and 2.450 eV, respectively. The band gap width of a semiconductor determines the charge transfer during the gas sensing process and the small forbidden bandwidth of S-AlTAG-0.6 reduced the obstruction of charge transfer.

Based on the calculation results of UPS and UV–vis DRS tests, the energy band schematic diagram is illustrated in **Figure 6**. It is apparent that S-AlT belongs to an n-type semiconductor and the nanohybrid is a p-type one through contrast to the relative position of their Fermi level, E_v, and E_c. This transition in semiconductor type that occurs after the assembly confirms the existence of a large-area heterojunction in the nanohybrid interface (**Figure 7**). In addition, this heterojunction "bridge" cross S-AlT and ANS-rGO leads to the energy bands bending and the forbidden bandwidth reduction in the nanohybrid, further inspiring a greater electron–hole pair separation. Specific binding between Fe—N_4 sites and NO ensures efficient and precise electron transfer to the latter, which will be manifested macroscopically through the sourcemeter as directional fluctuations in the electrical signals of the nanohybrid-based sensor. Comprehensively, the heterojunction model NO sensing mechanism can be explained as follows: The nanohybrid's heterojunction established through the hydrogen bond and the electrostatic interaction will reduce the band gap and the Fermi level, which essentially enables and facilitates the charge transfer from S-AlT to NO molecules during the sensing process. These advantages will be demonstrated by the high-speed response, low limit of detection, etc. of the gas sensing performance.

To further investigate the NO sensing mechanism, DFT calculation was established to understand the combining process of NO molecules to Fe—N_4 sites on Al-TCPP(Fe) MOFs at an atomic scale. **Figure 8a** exhibits the final optimized geometry among different orientations of NO molecule configuration bound on Al-TCPP(Fe) MOFs, suggesting that NO is vertically bonded to the iron atom at the center of the porphyrin plane in its axial direction, and the distance from the iron atom center of F—N_4 site to the nitrogen atom of NO is 1.8527 Å and the binding energy ΔE is −0.662 eV.[81] The charge density difference calculation (Figure 8b) illustrates the back donation of electrons from the iron atom center of the Fe—N_4 site to the nitrogen atom of NO,[32,82] and significantly, this back electron transfer interaction is not excessively strong so that the NO adsorption/desorption is readily reversible to achieve high-speed response/recovery performance.[81] Moreover, When NO is preset to bind with its oxygen atom to the iron atom of the Fe—N_4 site, the computational optimization results reveal that NO will flip and still bind with its nitrogen atom to the iron atom (Figure S23a,d, Supporting Information), confirming that the electron transfer tends to adopt the direction above mentioned during the sensing process. From the total density of states plot (Figure S24, Supporting Information), the electronic states do not cross the Fermi

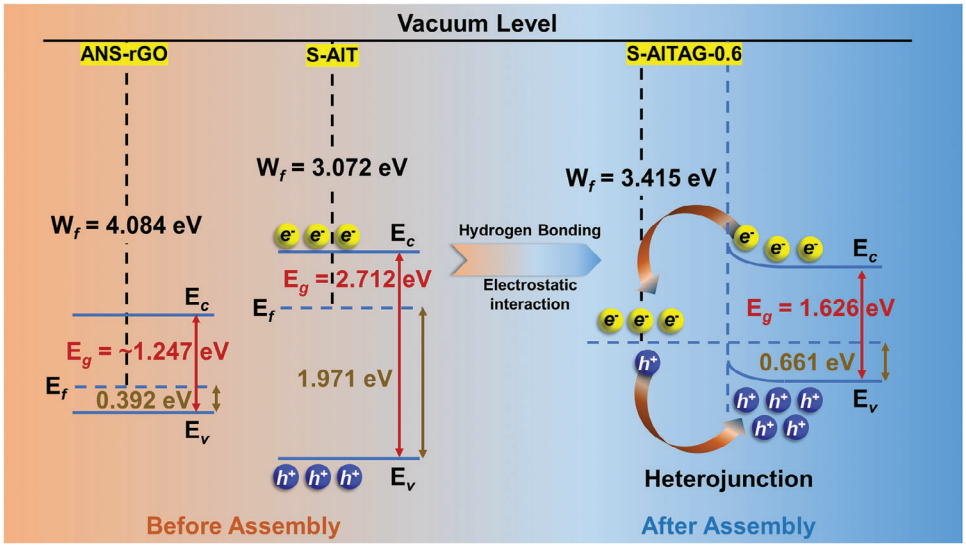

Figure 6. Energy band schematic diagram of ANS-rGO, S-AIT, and S-AITAG-0.6.

level, and the corresponding energy gap of Al-TCPP(Fe) MOFs is 2.414 eV,[67,72] which approximates the experimental value measured from UV–vis DRS. For the highly conductive ANS-rGO, ANS organic molecules as functionalized surface dopants can effectively modulate the electronic properties of rGO. The charge density difference calculation illustrates that the $-NH_2$ group of ANS molecule donates electrons to the $-SO_3H$ group and rGO, which increases the electron density on the surface as well as reduces the charge transfer barrier in the vacuum region of ANS-rGO.[40,42] ANS acts as a bridge with a donor-π-acceptor (D–π–A) structure, accelerating the electron transfer between NO and the nanohybrid, which facilitates the outstanding gas sensing properties of S-AITAG-0.6 based sensor.

2.5. Practical Detection of NO in Human Exhalation

According to relevant research, NO is the main volatile nitrogen oxide compound in human exhalation, and FeNO levels are typically less than 25 ppb in healthy individuals and more than 50 ppb in asthmatic patients.[6,7] It is reasonable to differentiate non-invasively between healthy individuals and asthmatic patients based on exhaled NO concentration. And S-AITAG-0.6 based sensor in this work can be designed as a platform for exhaled NO analysis with its superior NO sensing performance. During the exhaled NO analysis process, the resistive response of the sensor in this work is mainly contributed by NO. All exhalation samples were collected in 2 L aluminum foil gas collection bags, and the

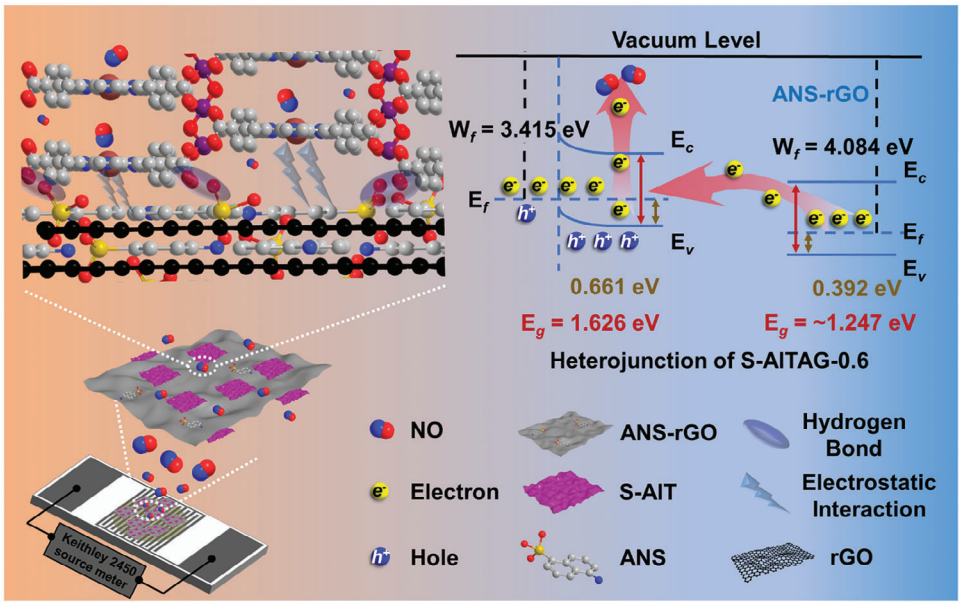

Figure 7. Schematic diagram of the gas sensing mechanism of S-AITAG-0.6 based sensor toward NO.

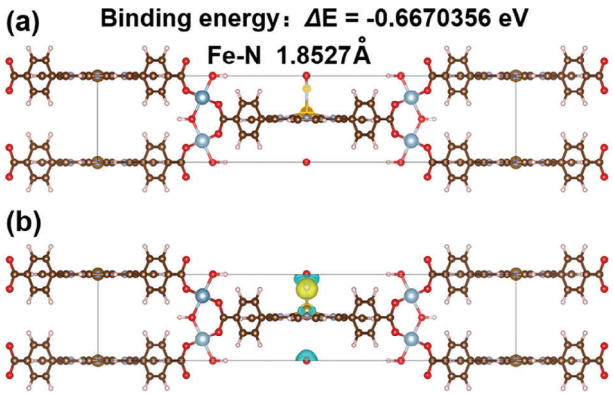

Figure 8. a) The optimized geometry of NO molecule configuration bound on Al-TCPP(Fe) MOF. b) Charge density difference plot of NO molecule bound on Al-TCPP(Fe) MOF. Yellow regions indicate electron accumulation and light blue regions stand for electron deficiency.

moisture in the collected gas was filtered through a simple pretreatment filter before testing. (Figure S26a–c, Supporting Information). All exhalation samples were obtained with the consent of volunteers (Tables S5, and S7, Supporting Information).

The five-cyclic response curve of the S-AlTAG-0.6 sensor of exhalation samples from healthy subjects is shown in Figure S27a (Supporting Information). To simulate the quantitative determination of NO concentration in the patient's exhalation samples, a certain of NO (10–100 ppb) was injected into the healthy subject's exhalation samples. The five-cycle response curves of the simulated patient's exhalation samples are shown in **Figure 9a**. A linear relationship between NO concentration and the response value was observed, with the linear fitting equation $y = 1.04565 + 0.00270x$ (Figure S27b, Supporting Information). It is clear from the box plot results that the sensor can successfully discriminate a healthy subject's exhalation from that of a simulated patient (Inset of Figure 9a). Furthermore, actual exhaled NO analysis was conducted on asthmatic patients, with the corresponding response curve and box plot shown in Figure 9b. Notably, the average exhaled NO concentration in asthmatic patients was 9.704 times higher than in healthy individuals. To the best of our knowledge, this is the first time reporting practical sensing measurement toward exhaled NO in asthma patients' breath at room temperature using chemiresistive materials. The results indicate that S-AlTAG-0.6-based sensor has the potential for diagnosing asthma and other inflammatory airway diseases in clinical settings.

3. Conclusion

In summary, we have successfully fabricated and demonstrated a prominent performance ppb-level NO chemiresistive gas sensors based on 3D spatial coordination Al-TCPP(Fe) MOFs with a modulated sheet morphology that arranged the organized activated Fe—N_4 sites. The ultrathin S-AlT, coordinated by the Al(OH)O_4 chain metal nodes and the TCPP(Fe) organic ligands, were assembly with the supramolecularly functionalized rGO sheets through the hydrogen bonding and the electrostatic interaction. The sensors based on S-AlTAG exhibited outstanding gas sensing performance toward NO at RT, particularly, the lowest limit of detection (R_a/R_g = 1.047, 5 ppb NO) reported so far among congeneric chemiresistive gas sensors. Further investigation to interpret the sensing mechanism, the NO sensing properties are substantiality enhanced through the synergistic combination of the abundant Fe—N_4 sites in the 3D entirety MOFs structure, the heterojunction, serving as an electron transport bridge spanning across S-AlTAG and the target gas molecules, the ultrathin sheet-on-sheet morphology superiority of S-AlT and the back donation behavior of electrons verified by the density functional theory calculations. Comprehensively, a plausible sensing mechanism based on charge transfer theory and energy band theory was developed. The intrinsic attributes of the high specific surface area and porosity endow S-AlT with preferable accumulation and mass transfer capabilities for target gas molecules, which will specifically bind with the Fe—N_4 sites orderly arranged in the 3D spatial coordination entirety network. While the heterojunction "bridge" interconnecting S-AlT to ANS-rGO will drop the nanohybrid's Fermi energy level and narrow the bandgap, which facilitates and accelerates the charge transfer process once the NO molecules bind upon the unoccupied Fe—N_4 sites, and the moderately strong charge transfer interactions ensures the NO molecules' adsorption/desorption can reverse readily to achieve high-speed response/recovery performance. Overall, the prominent performance is attributed to the thinner sheet-on-sheet morphology which benefits from the ultrathin MOF nanosheet built by morphological modulation, and larger area heterojunctions which benefit from the thinner sheet-on-sheet morphology built by hydrogen bonding and electrostatic interactions. The development of MOF/graphene sheet-on-sheet nanohybrids paves a new way for creating ultrahigh-performance gas sensing systems for trace NO monitoring, which is critical for practical FeNO fluctuation monitoring in clinical diagnosis and treatment.

4. Experimental Section

Materials: Aluminum chloride hexahydrate ($AlCl_3 \bullet 6H_2O$, 99.99%) and Cetyltrimethyl ammonium bromide (CTAB, ≥99%) were purchased from Innochem. 5-aminonaphthalene-1-sulfonic acid (ANS, 90%) was purchased from Alfa Aesar. Tetrakis (4-carboxyphenyl) porphyrin (TCPP, ≥98%) and Sodium hydroxide (NaOH, ≥98%) were purchased from Shanghai Titan Scientific Co., Ltd. Acetone (C_3H_6O, 99.5%), Hydrochloric acid ($HCl_{(aq)}$, 36%), Ferric chloride hexahydrate ($FeCl_3 \bullet 6H_2O$, ≥99%), and Hydrazine hydrate ($N_2H_4 \bullet H_2O$, ≥50%) were purchased from Guangzhou Chemical Reagent Factory Co., Ltd. N, N-Dimethylformamide (DMF, ≥99.5%), and Ethanol (C_2H_5OH, ≥99.7%) were purchased from Tianjin Zhiyuan Chemical Reagent Factory Co., Ltd. The graphene oxide (GO, 5.76 mg ml^{-1}, 325 mesh) aqueous solution was obtained by the modified Hummers' method with Graphite (see the Supporting Information for details). Deionized water was obtained with a Milli-Q Direct Water Purification System. All commercial chemicals were purchased without further purification unless otherwise mentioned.

Characterizations: The morphologies of the as-prepared samples were characterized by Field Emission Scanning Electron Microscopy (FESEM, FEI, Quanta 250 FEG, Germany). The TEM images were obtained by Transmission Electron Microscopy (TEM, JEOL, JEM-1400 PLUS, Japan). Atomic Force Microscopy (AFM, Multimode8) was used to measure the thickness and profile of S-AlT and ANS/rGO sheets in ScanAsyst mode. Energy dispersive X-ray spectroscopy (EDS) elemental mapping was analyzed by High-Angle Annular Dark-Field Scanning Transmission Electron Microscopy (HAADF STEM, FEI Talos F200X). The elemental composition of the as-prepared samples was characterized by an Inductively Coupled Plasma Optical Emission Spectrometer (ICP-OES, SPECTRO ARCOS

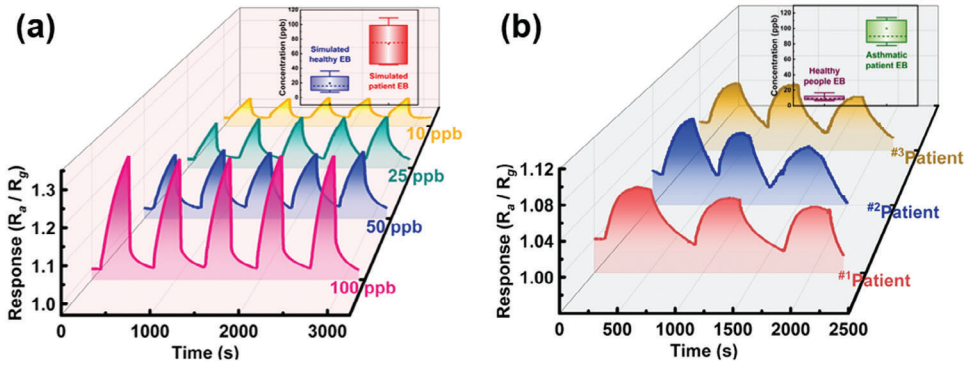

Figure 9. a) Five-cyclic response curve of S-AlTAG-0.6 based gas sensor toward exhalation samples from simulated patients with different NO concentrations. b) Three-cyclic response curve of S-AlTAG-0.6 based gas sensor toward exhalation samples from asthmatic patients. Box plot analysis of the differentiation capability of S-AlTAG-0.6-based sensor toward exhalation samples from healthy subjects versus simulated patients and healthy subjects versus asthmatic patients.

MV, Germany). The detailed structural properties of the as-prepared samples were characterized by Fourier Transform Infrared Spectroscopy (FTIR, Vertex 70, Bruker, Germany), and the X-ray diffraction (XRD) patterns of the as-prepared samples were obtained by using an X-ray diffractometer (XRD, D8 ADVANCE DAVINCI, Bruker, Germany) with Cu Kα radiation (λ = 1.54056 Å). The UV–vis absorption spectra were recorded in a UV–vis spectrophotometer (UV-1900, Shimadzu, Japan). The Raman spectra were obtained by Raman-scattering spectroscopy (Raman, Renishaw, UK) equipped with a 532 nm laser as an excitation source. A Zetapotential analyzer (Nanobrook 90 Plus PALS, Brookhaven, USA) was used to measure the Zeta potential of S-AlT and ANS/rGO aqueous solution. The elemental compositions and chemical bond information of the as-prepared samples were characterized by X-ray photoelectron spectroscopy (XPS, Shimadzu, Axis Supra, Japan) with a monochromatic Al/Ag dual anode X-ray source, and C 1s at 284.8 eV was used as a reference. UPS (Shimadzu, Axis Supra, Japan) was used to obtain the work function of the samples with a He I (21.2 eV) UV light source. The UV–vis diffuse reflectance spectra (UV–vis DRS) of the samples were measured by a UV–vis spectrophotometer (UV–vis, Shimadzu UV-2600). The N_2 adsorption/desorption isotherms were obtained using an automatic gas adsorption analyzer (ASAP 2460, Micromeritics Instrument Corp, USA). The relative humidity was controlled by a Gas and Liquid Distribution System with Humidity Control (DGL-III, ELITE TECH. China). The *I–V* characteristics curves of the sensors were recorded by a Keithley 2450 SourceMeter. Electrochemical impedance spectroscopy (EIS, SANQI, 1280HTDE-LTC, and Precise Impedance Analyzer, TH2851-050, Tonghui) was carried out to probe the charge transfer kinetics of the as-prepared samples.

Synthesis and Sensor Fabrication: GO aqueous solution was obtained by the modified Hummers' method, and GO was reduced by the hydrothermal method with hydrazine hydrate to get 5-aminonaphthalene-1-sulfonic acid modified reduced graphene oxide (ANS-rGO);[42] TCPP (Fe(III) *meso*-tetrakis (4-carboxylphenyl)) was prepared by the modified literature method;[66,67] The B-AlT and S-AlT crystals were synthesized through a hydrothermal method;[54,83] The synthesis process of C-AlT was similar to the above;[44] AlTAG Gas Sensing Materials were prepared through an ultrasound-assisted exfoliation method (see the Supporting Information for details).

Sensor Measurements: The obtained gas sensing materials were prepared into a gas sensor device by drop-casting method; As for the gas sensing analysis system, the electrical signal of the entire measurement process was monitored in real-time with a Keithley 2450 Sourcemeter, which reflected electrical conductivity variation caused due to the interaction between the sensing materials with NO. The pLOD was the lowest concentration of target gas that could be practically detected by the gas sensor device. Correspondingly, and the tLOD was calculated by the signal/noise ratio method[84] (see the Supporting Information for details).

Exhaled Nitric Oxide Analysis: The simulated exhaled NO analysis used the exhalation of a healthy subject as the background gas. All healthy subjects needed to meet requirements, including no smoking history, no alcohol or coffee consumption within 24 h, no eating for at least 2 h, and a gargling mouth before exhalation collection. The exhalation collection device included: disposable plastic mouthpieces, 2 L aluminum foil collection bags, sterile rubber tubing, double-valve U-shaped drying tubes, and color-changing silica gel. Prepare two U-shaped drying tubes filled with silica gel, the ends of which were connected to the mouthpiece and the collection bag, respectively. The healthy subjects needed to exhale slowly during collection so that the exhalation was sufficiently dried. This method could eliminate humidity interference. A simulated asthma patient's exhalation sample was prepared by injecting a certain concentration of standard NO into the healthy subject's exhalation sample. The above measurements were refered for the procedure of a complete simulated exhalation testing cycle.

The procedure of actual asthmatic patient exhaled NO analysis was as follows: the above gas sensing analysis system was operated, then injecting the 100 ml actual asthmatic patient's exhalation was injected into the 1000 ml nitrogen-filled test chamber, and the corresponding real-time sensing curve was obtained. All asthmatic patient's exhalation samples were collected at Zengcheng Campus, Nanfang Hospital, Southern Medical University, and the Ethics Committee of South China Academy of Advanced Optoelectronics, South China Normal University approved this study (SCNU-AOE-2023-206) on August 11, 2024.

Density Functional Theory (DFT) Calculation: The DFT calculation was carried out using the VASP package with the generalized gradient approximation and the Perdew–Burke–Ernzerhof exchange and correlation functional. The interactions between the ionic cores and the valence electrons were treated by ultrasoft pseudo potentials with atomic pseudo potentials corresponding to Al $3s^2 3p^1$ and Fe $3s^2 3p^6 3d^6 4s^2$. Zero damping DFT-D3 dispersion correction method of Grimme was used to account for the significance of Van der Waals (VdW) interactions of the adsorption between NO and interlayers of Al-TCPP(Fe) MOFs in the system. In all calculations, the cutoff energy of the plane wave was set at 520 eV and the Monkhorst Packk point was used to ensure that the total energy convergence criterion of the system reaches 10^{-5} eV Å^{-1}. Through DFT geometry optimization, the force acting on each atom was less than 0.02 eV, revealing the most stable adsorption configurations of Al-TCPP(Fe) MOFs with NO gas molecules.

Supporting Information

Supporting Information is available from the Wiley Online Library or from the author.

Acknowledgements

This work was supported by National Natural Science Foundation of China (Grant No.51973070), Guangdong Basic and Applied Basic Research Foundation (2022A1515010577, 2021A1515012420, 2023A1515010814), Startup Foundation from SCNU, Guangdong Provincial Key Laboratory of Optical Information Materials and Technology (2023B1212060065), the 111 Project., High-end Foreign Experts Recruitment Program (DL2023030001L), Calculations were made at Bianshui Riverside Supercomputing Center (BRSC).

Conflict of Interest

The authors declare no conflict of interest.

Author Contributions

Z.F. dealt with writing the review and editing, writing the original draft, visualization, methodology, investigation, formal analysis, and data curation, conceptualization. Y.C. dealt with the investigation. Z.C. dealt with writing the review and editing. H.X. dealt with writing the review and editing. Y.F. dealt with the theoretical calculation. F.W. dealt with conceptualization. H.L. dealt with conceptualization. Y.G. dealt with validation and funding acquisition. T.R. dealt with conceptualization. P.J.F. dealt with conceptualization. A.M.U.S. dealt with conceptualization. G.Z. dealt with conceptualization. Y.W. dealt with writing the review and editing, validation, supervision, resources, funding acquisition, and conceptualization.

Data Availability Statement

The data that support the findings of this study are available from the corresponding author upon reasonable request.

Keywords

heterojunctions, nitric oxide sensing, porphyrin MOFs, supramolecularly functionalized graphene, ultrathin sheet-on-sheet

Received: November 24, 2024
Revised: February 9, 2025
Published online: February 24, 2025

[1] L. E. Gustafsson, A. M. Leone, M. G. Persson, N. P. Wiklund, S. Moncada, *Biochem. Biophys. Res. Commun.* **1991**, *181*, 852.
[2] T. J. McMahon, R. E. Moon, B. P. Luschinger, M. S. Carraway, A. E. Stone, B. W. Stolp, A. J. Gow, J. R. Pawloski, P. Watke, D. J. Singel, C. A. Piantadosi, J. S. Stamler, *Nat. Med.* **2002**, *8*, 711.
[3] R. A. Dweik, P. B. Boggs, S. C. Erzurum, C. G. Irvin, M. W. Leigh, J. O. Lundberg, A.-C. Olin, A. L. Plummer, D. R. Taylor, A. T. S. C. Interpretat, *Am J. Respir. Crit. Care Med.* **2011**, *184*, 602.
[4] K. Alving, E. Weitzberg, J. M. Lundberg, *Eur. Respir. J.* **1993**, *6*, 1368.
[5] S.-I. Woo, J.-H. Lee, H. Kim, J.-W. Kang, Y.-H. Sun, Y.-S. Hahn, *Respir. Med.* **2012**, *106*, 1103.
[6] I. D. Pavord, D. E. Shaw, P. G. Gibson, D. R. Taylor, *Lancet* **2008**, *372*, 1017.
[7] A. Manolis, *Clin. Chem.* **1983**, *29*, 5.
[8] D. Yao, A. G. Vlessidis, N. P. Evmiridis, *Microchim. Acta.* **2004**, *147*, 1.
[9] A. J. Becker, S. Uckert, D. Tsikas, H. Noack, C. G. Stief, J. C. Frolich, G. Wolf, U. Jonas, *Urol. Res.* **2000**, *28*, 364.
[10] J. N. Bates, *NeuroProtocols* **1992**, *1*, 141.
[11] F. Bedioui, A. Ismail, S. Griveau, *Curr. Opin. Electrochem.* **2018**, *12*, 42.
[12] S. Uma, M. K. Shobana, *Sens. Actuators, A.* **2023**, *349*, 114044.
[13] M. Punginsang, A. Wisitsora-at, A. Tuantranont, S. Phanichphant, C. Liewhiran, *Sens. Actuators, B.* **2015**, *210*, 589.
[14] W. T. Koo, S. J. Choi, N. H. Kim, J. S. Jang, I. D. Kim, *Sens. Actuators, B* **2016**, *223*, 301.
[15] Y.-T. Tsai, S.-J. Chang, L.-W. Ji, Y.-J. Hsiao, I.-T. Tang, H.-Y. Lu, Y.-L. Chu, *ACS Omega* **2018**, *3*, 13798.
[16] E. Ciftyurek, Z. Li, K. Schierbaum, *Sensors* **2023**, *23*, 29.
[17] H. Ji, W. Zeng, Y. Li, *Nanoscale* **2019**, *11*, 22664.
[18] K. Cosby, K. S. Partovi, J. H. Crawford, R. P. Patel, C. D. Reiter, S. Martyr, B. K. Yang, M. A. Waclawiw, G. Zalos, X. Xu, K. T. Huang, H. Shields, D. B. Kim-Shapiro, A. N. Schechter, R. O. Cannon, M. T. Gladwin, *Nat. Med.* **2003**, *9*, 1498.
[19] T. Malinski, Z. Taha, *Nature* **1992**, *358*, 676.
[20] B. B. Wayland, L. W. Olson, *J. Am. Chem. Soc.* **1974**, *96*, 6037.
[21] Y. Gao, J. Wang, Y. Feng, N. Cao, H. Li, N. F. de Rooij, A. Umar, P. J. French, Y. Wang, G. Zhou, *Small* **2022**, *18*, 2103259.
[22] J. Wang, Y. Gao, F. Chen, L. Zhang, H. Li, N. F. de Rooij, A. Umar, Y.-K. Lee, P. J. French, B. Yang, Y. Wang, G. Zhou, *ACS Appl. Mater. Interfaces* **2022**, *14*, 53193.
[23] Z. Meng, A. Aykanat, K. A. Mirica, *J. Am. Chem. Soc.* **2019**, *141*, 2046.
[24] M. Zhao, Y. Wang, Q. Ma, Y. Huang, X. Zhang, J. Ping, Z. Zhang, Q. Lu, Y. Yu, H. Xu, Y. Zhao, H. Zhang, *Adv. Mater.* **2015**, *27*, 7372.
[25] W. Koo, J. Jang, I. Kim, *Chem* **2019**, *5*, 1938.
[26] M. G. Campbell, D. Sheberla, S. F. Liu, T. M. Swager, M. Dinca, *Angew. Chem., Int. Ed.* **2015**, *54*, 4349.
[27] Y. Yue, P. Cai, X. Xu, H. Li, H. Chen, H.-C. Zhou, N. Huang, *Angew. Chem., Int. Ed.* **2021**, *60*, 10806.
[28] Z. Yuan, H. Chai, Y. Huang, Z. Zhang, W. Tan, Y. Sun, J. Ma, G. Zhang, *Coord. Chem. Rev.* **2025**, *527*, 216385.
[29] L. He, Y. Liu, J. Liu, Y. Xiong, J. Zheng, Y. Liu, Z. Tang, *Angew. Chem., Int. Ed.* **2013**, *52*, 3741.
[30] H.-Y. Li, S.-N. Zhao, S.-Q. Zang, J. Li, *Chem. Soc. Rev.* **2020**, *49*, 6364.
[31] S.-S. Wang, H.-H. Huang, M. Liu, S. Yao, S. Guo, J.-W. Wang, Z.-M. Zhang, T.-B. Lu, *Inorg. Chem.* **2020**, *59*, 6301.
[32] S. Shang, W. Xiong, C. Yang, B. Johannessen, R. Liu, H.-Y. Hsu, Q. Gu, M. K. H. Leung, J. Shang, *ACS Nano* **2021**, *15*, 9670.
[33] H. He, J. Guo, J. Zhao, J. Xu, C. Zhao, Z. Gao, Y.-Y. Song, *ACS Sens.* **2022**, *7*, 2750.
[34] Y. Zhang, S. Lv, L. Jiang, F. Liu, J. Wang, Z. Yang, B. Wang, R. You, C. Wang, X. Yan, P. Sun, Y. Gao, X. Liang, G. Lu, *ACS Sens.* **2021**, *6*, 4435.
[35] L. Wang, X. Chen, Z. Yi, R. Xu, J. Dong, S. Wang, Y. Zhao, Y. Liu, *Small Methods* **2022**, *6*, 2200561.
[36] J. Qiu, X. Hu, X. Min, W. Quan, R. Tian, P. Ji, H. Zheng, W. Qin, H. Wang, T. Pan, S. Cheng, X. Chen, W. Zhang, X. Wang, *ACS Appl. Mater. Interfaces* **2020**, *12*, 19755.
[37] J. Liu, Y. Liu, H. Liu, Q. Pan, G. Zhang, *Sens. Actuators, B.* **2023**, *380*, 133308.
[38] G. Murali, M. Reddeppa, C.h. S. Reddy, S. Park, T. Chandrakalavathi, M.-D. Kim, I. In, *ACS Appl. Mater. Interfaces* **2020**, *12*, 13428.
[39] Z. Chen, J. Wang, N. Cao, Y. Wang, H. Li, N. F. de Rooij, A. Umar, Y. Feng, P. J. French, G. Zhou, *ACS Appl. Nano Mater.* **2021**, *4*, 13234.
[40] H. Liang, L. Guo, N. Cao, H. Hu, H. Li, N. Frans de Rooij, A. Umar, H. Algarni, Y. Wang, G. Zhou, *J. Mater. Chem. A.* **2021**, *9*, 23955.
[41] L. Guo, H. Liang, H. Hu, S. Shi, C. Wang, S. Lv, H. Yang, H. Li, N. F. de Rooij, Y.-K. Lee, P. J. French, Y. Wang, G. Zhou, *ACS Appl. Mater. Interfaces* **2023**, *15*, 18205.
[42] W. Pei, T. Zhang, Y. Wang, Z. Chen, A. Umar, H. Li, W. Guo, *Nanoscale* **2017**, *9*, 16273.
[43] Y. Chang, M. Chen, Z. Fu, R. Lu, Y. Gao, F. Chen, H. Li, N. Frans de Rooij, Y. K. Lee, Y. Wang, G. Zhou, *J. Mater. Chem. A.* **2023**, *11*, 6966.

[44] Y. Guo, S. Li, W. Abebe, J. Wang, L. Shi, D. Liu, S. Zhao, *Chin. J. Catal.* **2024**, *67*, 21.
[45] K. Jayaramulu, M. E. DMello, K. Kesavan, A. Schneemann, M. Otyepka, S. Kment, C. Narayana, S. B. Kalidindi, R. S. Varma, R. Zboril, R. A. Fischer, *J. Mater. Chem. A.* **2021**, *9*, 17434.
[46] Y. Wang, G. Zuo, J. Kong, Y. Guo, Z. Xian, Y. Dai, J. Wang, T. Gong, C. Sun, Q. Xian, *J. Hazard. Mater.* **2022**, *421*, 126634.
[47] J. Wu, J. Chen, C. Wang, Y. Zhou, K. Ba, H. Xu, W. Bao, X. Xu, A. Carlsson, S. Lazar, A. Meingast, Z. Sun, H. Deng, *Adv. Sci.* **2020**, *7*, 1903003.
[48] M. G. Campbell, S. F. Liu, T. M. Swager, M. Dinca, *J. Am. Chem. Soc.* **2015**, *137*, 13780.
[49] Y. Chang, J. Zhang, R. Lu, W. Li, Y. Feng, Y. Gao, H. Yang, F. Wang, H. Li, Y.-K. Lee, P. J. French, A. M. Umar Siddiqui, Y. Wang, G. Zhou, *J. Mater. Chem. C.* **2024**, *12*, 7520.
[50] S. Moribe, Z. Chen, S. Alayoglu, Z. H. Syed, T. Islamoglu, O. K. Farha, *ACS Mater. Lett.* **2019**, *1*, 476.
[51] Y. Xiao, W. Guo, H. Chen, H. Li, X. Xu, P. Wu, Y. Shen, B. Zheng, F. Huo, W. D. Wei, *Mater. Chem. Front.* **2019**, *3*, 1580.
[52] Z. Wang, J. Zhu, S. Xu, Y. Zhang, B. Van der Bruggen, *J. Membr. Sci.* **2021**, *633*, 119397.
[53] Z. Zhang, Y. Wang, B. Niu, B. Liu, J. Li, W. Duan, *Nanoscale* **2022**, *14*, 7146.
[54] A. Fateeva, P. A. Chater, C. P. Ireland, A. A. Tahir, Y. Z. Khimyak, P. V. Wiper, J. R. Darwent, M. J. Rosseinsky, *Angew. Chem., Int. Ed.* **2012**, *51*, 7440.
[55] Y. Liang, W. Hu, X. Yuan, Z. Zeng, B. Zhu, Y. Gu, *Adv. Opt. Mater.* **2022**, *10*, 2200779.
[56] Y. Zhao, J. Wang, R. Pei, *J. Am. Chem. Soc.* **2020**, *142*, 10331.
[57] J. Liu, W. Zhou, J. Liu, Y. Fujimori, T. Higashino, H. Imahori, X. Jiang, J. Zhao, T. Sakurai, Y. Hattori, W. Matsuda, S. Seki, S. K. Garlapati, S. Dasgupta, E. Redel, L. Sun, C. Wöll, *J. Mater. Chem. A.* **2016**, *4*, 12739.
[58] R. Buntem, A. Intasiri, W. Lueangchaichaweng, *J. Colloid Interface Sci.* **2010**, *347*, 8.
[59] S. Zakavi, S. Talebzadeh, S. Rayati, *Polyhedron* **2012**, *31*, 368.
[60] C. Li, M. Song, S. Wu, Z. Wang, N. Duan, *Talanta* **2023**, *251*, 123739.
[61] M. Liu, Y. J. Chen, X. Huang, L. Z. Dong, M. Lu, C. Guo, D. Yuan, Y. Chen, G. Xu, S. L. Li, Y. Q. Lan, *Angew. Chem., Int. Ed.* **2022**, *61*, 202115308.
[62] H. Huang, Z. Yue, G. Li, X. Wang, J. Huang, Y. Du, P. Yang, *J. Mater. Chem. A.* **2014**, *2*, 20118.
[63] B. Vlckova, P. Matejka, J. Simonova, K. Cermakova, P. Pancoska, V. Baumruk, *J. Phys. Chem.* **1993**, *97*, 9719.
[64] W. Zhao, J. Peng, W. Wang, B. Jin, T. Chen, S. Liu, Q. Zhao, W. Huang, *Small* **2019**, *15*, 1901351.
[65] X. Huang, P. Oleynikov, H. He, A. Mayoral, L. Mu, F. Lin, Y. B. Zhang, *Nano Res.* **2022**, *15*, 145.
[66] B. Yao, C. Peng, W. Zhang, Q. Zhang, J. Niu, J. Zhao, *Appl. Catal. B.* **2015**, *77*, 174.
[67] M. Cong, X. Chen, K. Xia, X. Ding, L. Zhang, Y. Jin, Y. Gao, L. Zhang, *J. Mater. Chem. A.* **2021**, *9*, 4673.
[68] Y. Xu, H. Bai, G. Lu, C. Li, G. Shi, *J. Am. Chem. Soc.* **2008**, *130*, 5856.
[69] X. Wei, J. Tian, C. Wang, S. Cheng, X. Fei, F. Yin, L. Xu, Y. Li, *J. Colloid Interface Sci.* **2025**, *680*, 66.
[70] M.-S. Yao, J.-W. Xiu, Q.-Q. Huang, W.-H. Li, W.-W. Wu, A.-Q. Wu, L.-A. Cao, W.-H. Deng, G.-E. Wang, G. Xu, *Angew. Chem., Int. Ed.* **2019**, *58*, 14915.
[71] C. Tang, Y. Li, X. Fei, W. Zhao, J. Tian, L. Xu, Y. Wang, *J. Colloid Interface Sci.* **2025**, *680*, 1030.
[72] H. Cheng, J. Wang, Y. Yang, H. Shi, J. Shi, X. Jiao, P. Han, X. Yao, W. Chen, X. Wei, P. K. Chu, X. Zhang, *Small* **2022**, *18*, 2200857.
[73] M. Jana, P. Khanra, N. C. Murmu, P. Samanta, J. H. Lee, T. Kuila, *Phys. Chem. Chem. Phys.* **2014**, *16*, 7618.
[74] G. Li, T. Yan, H. Zhao, D. Liu, *J. Solid State Chem.* **2023**, *317*, 123659.
[75] Y. Li, Z. Gao, F. Chen, C. You, H. Wu, K. Sun, P. An, K. Cheng, C. Sun, X. Zhu, B. Sun, *ACS Appl. Mater. Interfaces* **2018**, *10*, 30930.
[76] Z. Chen, P. Yuan, C. Chen, X. Wang, J. Wang, J. Jia, B. Davaasuren, Z. Lai, N. M. Khashab, K.-W. Huang, O. M. Bakr, J. Yin, K. N. Salama, *Adv. Mater.* **2024**, *36*, 2404291.
[77] M. Hakim, Y. Y. Broza, O. Barash, N. Peled, M. Phillips, A. Amann, H. Haick, *Chem. Rev.* **2012**, *112*, 5949.
[78] J. D. Pleil, M. A. Stiegel, T. H. Risby, *J. Breath Res.* **2013**, *7*, 017107.
[79] N. Zhang, Y.-G. Luo, Y.-H. Chen, J.-Y. Zhang, H. Wang, Z.-J. Liu, *ACS Sustainable Chem. Eng.* **2023**, *11*, 4813.
[80] Y. Wang, R. Tu, C. Hou, Z. Wang, *J. Solid State Electrochem.* **2022**, *26*, 565.
[81] S. Shang, C. Yang, C. Wang, J. Qin, Y. Li, Q. Gu, J. Shang, *Angew. Chem., Int. Ed.* **2020**, *59*, 19680.
[82] F. Leng, H. Liu, M. Ding, Q. P. Lin, H. L. Jiang, *ACS Catal.* **2018**, *8*, 4583.
[83] Y. Xiao, C. Chen, Y. Wu, J. Wang, Y. Yin, J. Chen, X. Huang, P. Qi, B. Zheng, *Microporous Mesoporous Mater.* **2021**, *324*, 111272.
[84] S. Ammu, V. Dua, S. R. Agnihotra, S. P. Surwade, A. Phulgirkar, S. Patel, S. K. Manohar, *J. Am. Chem. Soc.* **2012**, *134*, 4553.